

# Parameterization Improvements in an Eddy-Permitting Ocean Model for Climate

PETER R. GENT AND ANTHONY P. CRAIG

*National Center for Atmospheric Research, Boulder, Colorado*

CECILIA M. BITZ

*Polar Science Center, Applied Physics Laboratory, Seattle, Washington*

JOHN W. WEATHERLY

*Cold Regions Research and Engineering Laboratory, Hanover, New Hampshire*

(Manuscript received 21 May 2001, in final form 26 November 2001)

## ABSTRACT

Different parameterizations for vertical mixing and the effects of ocean mesoscale eddies are tested in an eddy-permitting ocean model. It has a horizontal resolution averaging about  $0.7^\circ$  and was used as the ocean component of the parallel climate model. The old ocean parameterizations used in that coupled model were replaced by the newer parameterizations used in the climate system model. Both ocean-alone and fully coupled integrations were run for at least 100 years. The results clearly show that the drifts in the upper-ocean temperature profile using the old parameterizations are substantially reduced in both sets of integrations using the newer parameterizations. The sea-ice distribution in the fully coupled integration using the newer ocean parameterizations is also improved. However, the sea-ice distribution is sensitive to both sea-ice parameterizations and the atmospheric forcing, in addition to being dependent on the ocean simulation. The newer ocean parameterizations have been shown to improve considerably the solutions in non-eddy-resolving configurations, such as in the climate system model, where the horizontal resolution of the ocean component is about  $2^\circ$ . The work presented here is a clear demonstration that the improvements continue into the eddy-permitting regime, where the ocean component has an average horizontal resolution of less than  $1^\circ$ .

## 1. Introduction

Projections of the earth's climate over the next century are often simulated with coupled climate models consisting of atmosphere, land, ocean, and sea-ice components. These projections are more plausible if the climate model does not drift when control simulations are made without the use of flux adjustments. This is the case with some climate models, such as the climate system model (CSM) (see Boville and Gent 1998), and version three of the Hadley Centre coupled model (HadCM3) (see Gordon et al. 2000). Both papers conclude that a very important factor contributing to this success is improved mixing parameterizations in the ocean component, which maintain an accurate temperature profile in the upper ocean and produce a realistic poleward heat transport. This is also very important in order to obtain the correct projected change in sea level, because it depends nonlinearly on the upper-ocean temperature profile of the control simulation.

The CSM consists of atmosphere, ocean, land, and sea-ice components. The atmosphere component is the Community Climate Model version 3 (CCM3), and the land component is the National Center for Atmospheric Research (NCAR) land surface model, both run at T42 resolution. The CSM sea-ice component consists of the cavitating-fluid rheology plus a simple three-layer thermodynamics, and uses the same grid as the ocean component. The ocean component is non-eddy-resolving because it has a horizontal resolution averaging about  $2^\circ$  (see Gent et al. 1998). One of the new parameterizations in this component represents the effect of unresolved ocean eddies on the mean state, due to Gent and McWilliams (1990). This new parameterization, with the Visbeck et al. (1997) modification described in section 2, is also used in the HadCM3 coupled model, where the horizontal resolution of the ocean component is  $1.25^\circ$ . Thus, an important question is whether this parameterization is still needed when the ocean component has higher horizontal resolution, which permits considerable eddy activity. Roberts and Marshall (1998) answer this question in the affirmative, but they only performed ocean-alone experiments in an idealized

---

*Corresponding author address:* Dr. Peter R. Gent, NCAR, P.O. Box 3000, Boulder, CO 80307-3000.  
E-mail: gent@ucar.edu

ocean basin. This question has not been addressed before in fully coupled climate models.

For example, the ocean component of the parallel climate model (PCM), which has quite high horizontal resolution averaging about  $0.7^\circ$ , did not use this parameterization. The PCM atmosphere and land components are the same as in the CSM, run at the same resolution. The PCM sea-ice component differs from that in the CSM, is run on a different grid than the ocean component, and is documented in Washington et al. (2000). When run in fully coupled mode, the ocean component of the PCM lost a considerable amount of heat. Figure 3 of Meehl et al. (2001) shows that the PCM is  $2.5^\circ\text{C}$  colder than observations between the surface and 400 m along the equator in the Pacific Ocean. This bias is smaller in the ocean component of the CSM. Therefore, the question arose as to whether the ocean mixing parameterizations used in the CSM would help reduce the bias in the upper ocean of the PCM.

Two sets of integrations were performed to address this question. The first set comprises ocean-alone integrations using a repeating annual cycle of forcing taken from observations. The second set comprises two fully coupled integrations that differ only in their ocean mixing parameterizations. The ocean model and parameterizations are described in section 2. The ocean-alone setup and results are presented in section 3, and the fully coupled setup and results are presented in section 4. Section 5 contains the discussion and conclusions.

## 2. Ocean model and parameterizations

The ocean model uses the Parallel Ocean Program (POP) code, which was developed at the Los Alamos National Laboratory (see Smith et al. 1992). The ocean grid uses spherical coordinates in the Southern Hemisphere, but in the Northern Hemisphere the pole is displaced to  $50^\circ\text{N}$ ,  $95^\circ\text{W}$ . The horizontal grid used  $384 \times 288$  grid points, and the resolution is nonuniform in both grid directions. The zonal resolution is finest at the longitude of the displaced pole, where it is  $0.6^\circ$ , and is coarsest at  $85^\circ\text{E}$ , where it is  $1.1^\circ$ . In the Southern Hemisphere, the meridional resolution is  $0.5^\circ$  at the equator, gradually increasing to a maximum of  $0.9^\circ$  at  $30^\circ\text{S}$ , and then decreasing to  $0.3^\circ$  near Antarctica. This choice is to give high resolution at the equator and to keep the grid boxes relatively square elsewhere. The horizontal grid is shown in Fig. 1 of Washington et al. (2000). There are 32 levels in the vertical; the first four in the upper ocean are 25 m thick, and below 100 m the resolution coarsens, with the bottom level being 300 m thick. The minimum ocean depth is 50 m, and the maximum depth is 5.1 km. The standard horizontal viscosity is a biharmonic operator with the coefficient depending on the square of the gridbox area. At the equator the coefficient varies between  $-10$  and  $-25 \times 10^{10} \text{ m}^4 \text{ s}^{-1}$ .

### a. Vertical mixing

The vertical mixing in the PCM-1 is the scheme of Pacanowski and Philander (1981, hereafter PP81). This was originally designed for tropical ocean models where the strong velocity shears in the vertical produce small gradient Richardson numbers. The vertical viscosity and diffusivity increase as the Richardson number decreases, using the same functional forms as in the original paper. The background values, to which the vertical viscosity and diffusivity tend when the Richardson number is large, are  $1.0$  and  $0.1 \text{ cm}^2 \text{ s}^{-1}$ , respectively. When using the PP81 mixing scheme, convective adjustment also has to be explicitly parameterized; otherwise the model does not maintain a stable vertical density profile in the deep ocean. Deep water formation is accomplished by the convective adjustment parameterization in this model configuration.

The new vertical mixing scheme is the K-profile parameterization (KPP) scheme of Large et al. (1994). This parameterizes the effects of several physical mechanisms in addition to shear mixing and was designed to work at middle and high latitudes, as well as in the Tropics. This scheme was used in the ocean component of the CSM (see Gent et al. 1998), and the same parameter values are used in this study. In particular, the internal wave, or background, values of the vertical viscosity and diffusivity are again  $1.0$  and  $0.1 \text{ cm}^2 \text{ s}^{-1}$ . In this model configuration, convective adjustment is not needed because there is a stable vertical density profile everywhere below the boundary layer, and the KPP mixing scheme allows deep water formation to take place when the diagnosed boundary layer depths are very large.

### b. Effects of mesoscale eddies

The original parameterization of the effects of mesoscale eddies on the potential temperature and salinity in the PCM-1 is horizontal biharmonic mixing. This mixing coefficient also depends upon the square of the gridbox area, and at the equator it varies between  $-1.0$  and  $-2.5 \times 10^{10} \text{ m}^4 \text{ s}^{-1}$ . It is well known that this parameterization diffuses density in adiabatic conditions, which results in poor simulations of potential temperature and salinity in the deep ocean in long integrations to equilibrium.

The second parameterization of the effects of mesoscale eddies is that of Gent and McWilliams (1990, hereafter GM90), which mixes along isopycnals with a Laplacian operator, and uses an additional advection of temperature and salinity. This scheme was also used in the ocean component of the CSM (see Gent et al. 1998), with the same constant parameter value in the mixing and advection terms. In this implementation, a smaller globally constant parameter value of  $100 \text{ m}^2 \text{ s}^{-1}$  is used in both terms, because of the higher horizontal resolution.

The third parameterization used in this study is the modification of the GM90 scheme proposed by Visbeck et al. (1997, hereafter VMHS). This scheme has the GM90 coefficient varying with time and horizontal position depending upon the local baroclinicity of the ocean model flow. The VMHS coefficient is evaluated as

$$\kappa_{\text{VMHS}} = \alpha |f| l^2 / (\text{Ri})^{1/2}, \quad (1)$$

where  $\alpha = 0.015$ , and  $f$  is the Coriolis parameter. Visbeck et al. (1997) choose the length scale  $l$  to be the width of the baroclinic zone but also mention that it could be the Rossby radius of deformation. We made the second choice, bounded below by the shortest side of a grid box, because otherwise the coefficient would be quite small in the Tropics due to the Coriolis term. The gradient Richardson number  $\text{Ri}$  and the vertical density gradient to determine  $l^2$  in Eq. (1) are evaluated at all interfaces over the depth range of 50 m–1 km, or over fewer levels if the ocean depth is less than 1 km, and averaged in the vertical. In addition, upper and lower limits of 500 and 50  $\text{m}^2 \text{s}^{-1}$ , respectively, are imposed on the value of  $\kappa_{\text{VMHS}}$ ; it is evaluated once a day, not every time step.

### 3. Ocean-alone setup and results

Four ocean-alone integrations were performed, each lasting at least 100 yr. A repeating annual cycle of forcing was used, which is described in detail in appendix A of Large et al. (1997). The wind stress is prescribed from the National Centers for Environmental Prediction (NCEP) reanalysis fields, but the heat and freshwater fluxes both depend upon the model sea surface temperature (SST) through the standard formulas. The observed downward solar radiation and reanalyzed relative humidity were both modified so that the annually averaged, global heat flux balanced to less than  $1 \text{ W m}^{-2}$ , when evaluated using an observed climatology for the SST. The strong negative feedbacks in the surface heat flux formulas then ensure that the area-averaged SST cannot drift very far from the observed value in ocean-alone integrations such as these. However, this constraint does not apply to the sea surface salinity when it is forced by an observed precipitation field minus evaporation. The reasons are that the freshwater flux does not contain negative feedbacks, and precipitation over the World Ocean is not known to great accuracy. This results in the need for a time-varying factor multiplying the precipitation field, and a weak, open ocean restoring term with a timescale of 6 months over 50 m in the freshwater flux formulation (see appendix A of Large et al. 1997). These terms are necessary in order to prevent drift in equilibrium integrations and can be considered as modifications of the observed precipitation and river runoff fields (see section 7 of Gent et al. 1998). Finally, in these integrations the effects of sea ice are parameterized by strong restoring with a timescale of 6 days to observed SST and sea surface salinity

in areas diagnosed as covered by sea ice. The four integrations are

- (A) The original model formulation with PP81 vertical mixing and biharmonic horizontal mixing of tracers;
- (B) KPP vertical mixing and biharmonic horizontal mixing of tracers;
- (C) KPP vertical mixing and the GM90 mesoscale eddy parameterization;
- (D) KPP vertical mixing and the VMHS modification of the GM90 scheme.

All four integrations were started with temperature and salinity values from the Levitus et al. (1994) annual mean data and from a state of rest. After 100 or so years of integration, at most only the upper kilometer of the ocean has reached equilibrium because of the small vertical diffusivity values below the strong mixing that occurs in the upper ocean. Because the area-averaged SST is strongly constrained, this means that the best place to analyze drifts in these integrations is the temperature profile down to about 1 km. The sea surface salinities can drift in time, so the salinity profile is less useful to analyze drifts, but is still instructive.

Figure 1 shows the time evolution of the area-averaged temperature at the surface and depths of 147, 289, and 520 m from the four integrations. Figure 1a shows that, after 100 yr, the area-averaged SST in all four integrations is very close to  $18^\circ\text{C}$ . Figure 1b shows that none of the cases drifted much at all at 147 m, with the largest drift being a  $0.2^\circ\text{C}$  cooling in cases C and D from the Levitus value of  $13.4^\circ\text{C}$ . In fact, the four potential temperature profiles remain close to each other and to observations down to about 200 m. However, between this depth and 1 km, where mixing is much weaker than near the surface, the temperature profiles diverge. Figures 1c,d show that the largest drifts occur at 289 and 520 m in the original ocean model configuration, case A. After 100 yr, case A has warmed by  $1^\circ\text{C}$  at 289 m from the Levitus value of  $10.2^\circ\text{C}$ , and at 520 m it has warmed by  $1.3^\circ\text{C}$  from the Levitus value of  $7.2^\circ\text{C}$ . The drift is only reduced a little in case B, when the PP81 vertical mixing scheme is replaced by the KPP scheme. However, the drift is almost eliminated in cases C and D when the GM90 or VMHS schemes replace the biharmonic mixing of tracers. There is little to choose between the last two schemes in global measure, but there are regional differences between the two cases that will be discussed below.

There is also a significant difference between cases A and B and cases C and D in the globally averaged temperature trends and the annual average poleward heat transport by the mean flow, which are shown in Fig. 2. Figure 2a shows that the globally averaged temperature in cases A and B has increased by  $0.4^\circ\text{C}$  after 100 yr, whereas in cases C and D it has decreased by  $0.05^\circ\text{C}$ . This is consistent with previous results implementing the GM90 parameterization in a model with  $3^\circ$

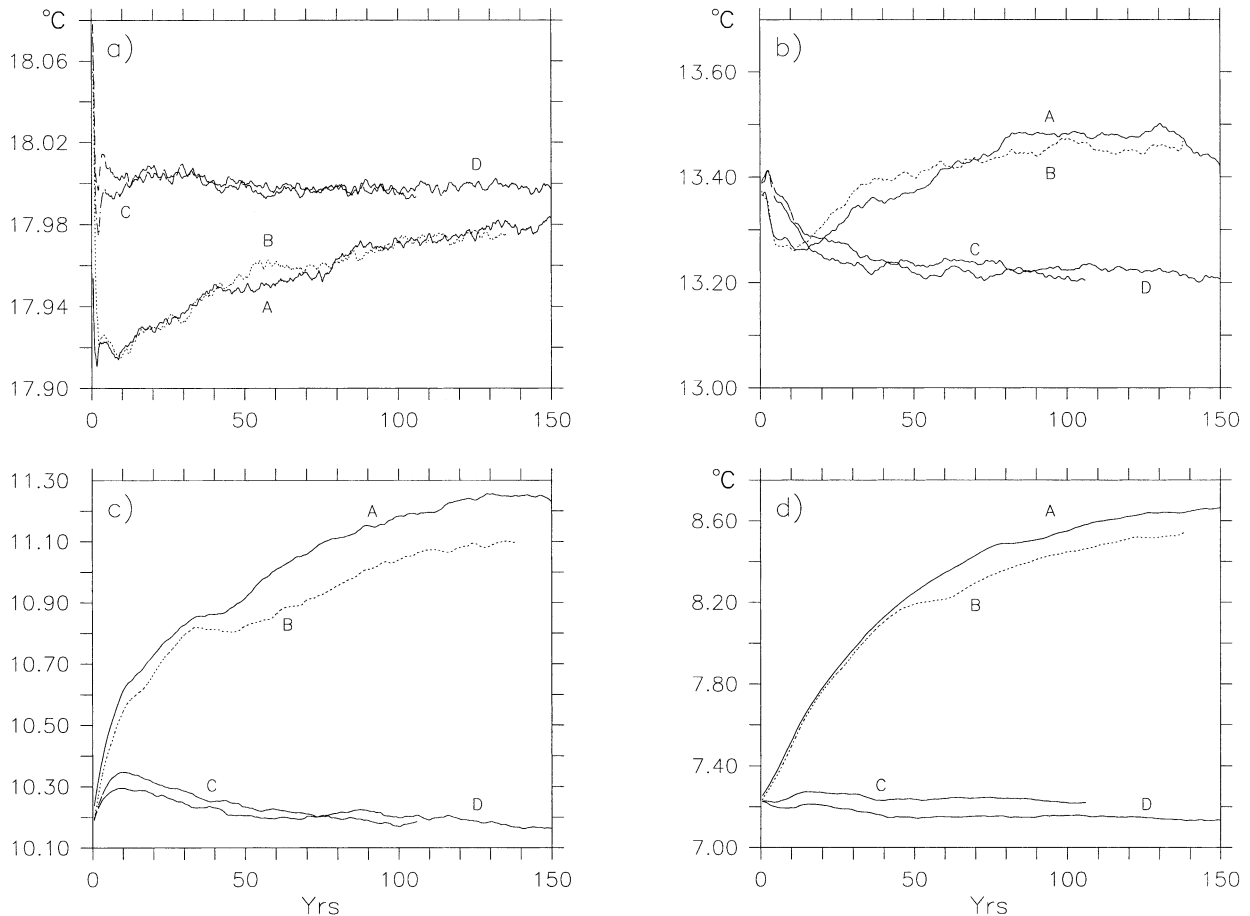


FIG. 1. The area-averaged potential temperature ( $^{\circ}\text{C}$ ) at depths of (a) 0, (b) 147, (c) 289, and (d) 520 m from the four ocean-alone integrations plotted against time (yr).

horizontal resolution (see Fig. 2 of Large et al. 1997). However, the trends in cases A and B, using higher resolution, are considerably smaller than in the  $3^{\circ}$  model. It can be deduced from Fig. 2a that the poleward heat transport from the ocean model and that calculated from the surface fluxes in cases C and D will be very close. This is less true in cases A and B because of the trend in the global temperature. Figure 2b shows that there are small differences in the northern subtropics in the poleward heat transports, and the maximum value in all four cases is close to 2 PW. This is very close to the best estimates using both direct ocean observations (see Hall and Bryden 1982; Bryden et al. 1991), and residuals from atmospheric estimates (see Trenberth and Caron 2001). However, there are more significant differences in the Southern Hemisphere between the equator and  $60^{\circ}\text{S}$ . The meridional heat transport is much weaker in cases A and B, and the transport is toward the equator between  $25^{\circ}$  and  $47^{\circ}\text{S}$ . In cases C and D the heat transport is stronger, and is equatorward only between  $40^{\circ}$  and  $45^{\circ}\text{S}$ . This is precisely the region where the heat transport by the eddies using the GM90 scheme is largest, and it is poleward [e.g., see Fig. 8 of Dan-

abasoglu (1998)]. Unfortunately, the diagnostics required to evaluate the eddy-induced circulation and its poleward heat transport were not saved, so that the total advective heat transport in cases C and D cannot be evaluated. However, it is likely poleward everywhere in the Southern Hemisphere in cases C and D, which is consistent with both direct ocean observations (see Macdonald and Wunsch 1996) and residuals from atmospheric estimates (see Trenberth and Caron 2001).

Figure 3 shows the average salinity profile down to 3 km at year 100 from the four integrations, plus the profile from Levitus et al. (1994). All four integrations have become significantly fresher at the surface, and the freshening drift continues down to about 600 m. This results in a significant underestimate of the salinity maximum at about 200-m depth in all model integrations. Below about 600 m, all the cases are too saline and underestimate somewhat the salinity minimum at about 800-m depth. Cases C and D have larger drifts than cases A and B both above 500 m and below 1 km, and none of the salinity profiles is very good. However, it is much more difficult to interpret the trends in the upper ocean salinity profile than the heat profile. The reasons

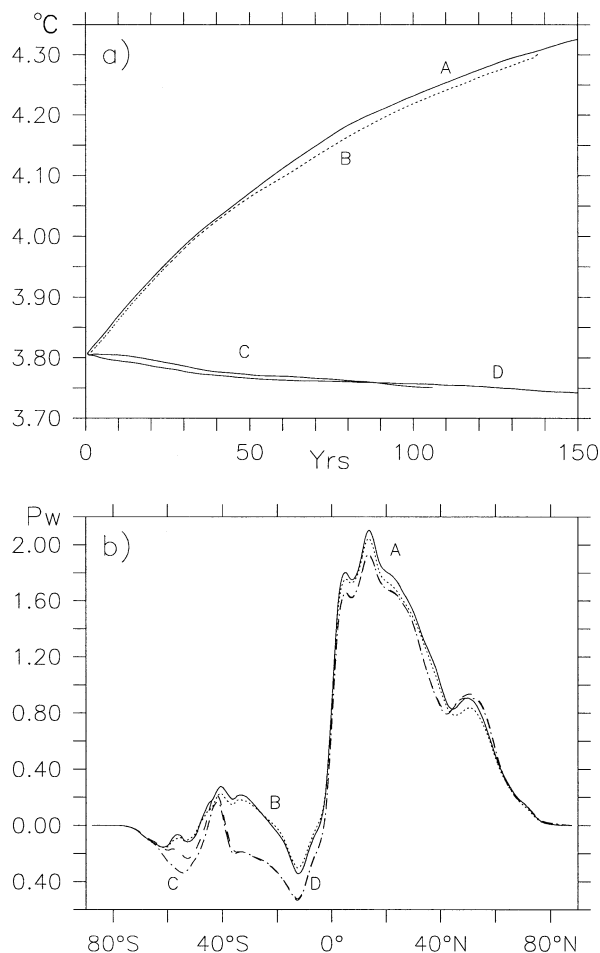


FIG. 2. (a) The globally averaged potential temperature ( $^{\circ}\text{C}$ ) plotted against time (yr), and (b) the annual average poleward heat transport (PW) by the mean flow at year 100 from the four ocean-alone integrations.

are that the surface freshwater forcing is not known very precisely, and there is a lack of feedbacks by the surface salinity on the surface flux laws. Thus, small drifts in the salinity field can persist over time and produce quite large salinity biases. Eliminating this drift remains to be solved adequately in long, equilibrium ocean-alone integrations.

The VMHS scheme has not been used very frequently in ocean climate models, so it is interesting to look at the differences it makes compared to using a constant coefficient in the GM90 mixing scheme, case C. A typical distribution of  $\kappa_{\text{VMHS}}$ , defined in Eq. (1), from case D is shown in Fig. 4. The figure shows that the isopycnal diffusivity takes large values in the Tropics, along western boundaries, and in the region of the Antarctic Circumpolar Current (ACC). The diffusivity also takes its minimum value in a large percentage of the ocean, where the flows and baroclinicity are weaker. The pattern in the North Atlantic can be compared to the eddy kinetic energy from a  $0.1^{\circ}$  calculation, which is shown

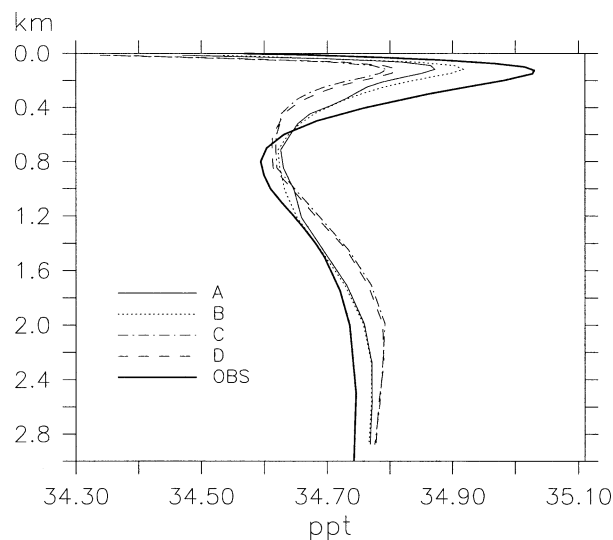


FIG. 3. The area-averaged salinity profile (in parts per thousand) down to 3 km at year 100 from the four ocean-alone integrations, and the Levitus et al. observations.

in Fig. 15b of Smith et al. (2000). The comparison is quite good, although in the high-resolution model the eddy energy in the Gulf Stream is higher than in the Tropics, whereas the coefficient in Fig. 4 is of comparable magnitude in these two regions.

The temperature distribution in the upper 500 m has equilibrated after 100 years of integration, so this is where to look for differences between cases C and D. The largest changes in SST occur in the ACC region, the far North Atlantic, and in the Greenland-Iceland-Norwegian (GIN) Sea. These are also the regions of largest temperature change throughout the upper 500 m. The annual average temperature difference at 520 m between cases C and D after 100 yr is shown in Fig. 5. The changes are mostly in the range of  $\pm 3^{\circ}\text{C}$  and are the result of small meridional displacements in regions of strong temperature gradients. These changes occur

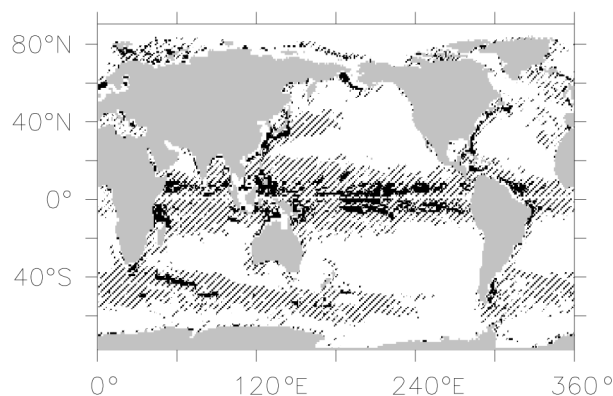


FIG. 4. A typical distribution of the isopycnal diffusivity coefficient in case D using the VMHS parameterization. Hatched areas are  $>100 \text{ m}^2 \text{ s}^{-1}$ , and solid black areas are  $>400 \text{ m}^2 \text{ s}^{-1}$ .

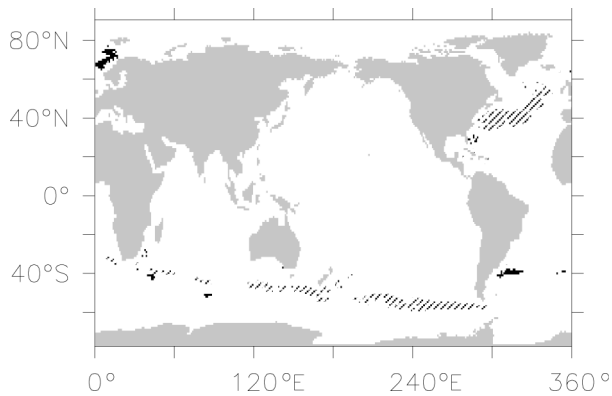


FIG. 5. Annual average potential temperature difference at 520-m depth and year 100 between cases D and C. Hatched areas are  $< -1^{\circ}\text{C}$ , and solid black areas are  $> 1^{\circ}\text{C}$ .

where  $\kappa_{\text{VMHS}}$  from Fig. 4 is large away from the Tropics. An exception is the Kuroshio region in the west Pacific, where the diffusivity is large, but it makes very little temperature change. The other region where the large diffusivity makes little difference is in the Tropics. Here, the circulation is mostly directly forced and so depends more on the wind stress and the heat and water fluxes than on the value of the isopycnal diffusivity coefficient.

However, by far the largest difference between cases C and D after 100 years occurs in the meridional overturning streamfunction calculated from the mean flow, which excludes the eddy-induced circulation. Figure 6a shows the annual average streamfunction from case D, and the difference between cases D and C is shown in Fig. 6b. Figure 6b shows that the largest difference occurs at  $36^{\circ}\text{S}$ , 3.7-km depth, and is 4.5 Sverdrups (Sv;  $1 \text{ Sv} \equiv 10^6 \text{ m}^3 \text{ s}^{-1}$ ), which reduces the strength of this deep overturning cell from  $-15.5 \text{ Sv}$  in case C to  $-11 \text{ Sv}$  in case D. This is a significant change, but a caveat is that the ocean at this depth has not yet reached an equilibrium solution. However, the weaker deep overturning cell in case D, shown in Fig. 6a, is more consistent with ocean observations. This cell, which brings deep Antarctic Bottom Water north, occurs mainly in the Atlantic Ocean. McCartney and Curry (1993) estimate that about 5 Sv of Antarctic Bottom Water flows north across the equator in the Atlantic. Case D has a stronger eddy meridional overturning circulation in the ACC region than case C, because of the large values of  $\kappa_{\text{VMHS}}$  there (see Fig. 4). This stronger eddy activity leads to an increased meridional flattening of the isopycnals and, hence, to a smaller ACC transport in case D. This dependence of the ACC transport on the value of the isopycnal diffusivity is examined in more detail in Gent et al. (2001). The Drake Passage transport is 5 Sv smaller in case D than case C at the end of the 100-yr integrations. In summary, the largest differences between cases C and D occur in the same regions where changing to the GM90 parameterization from the older physics of horizontal tracer mixing made the largest

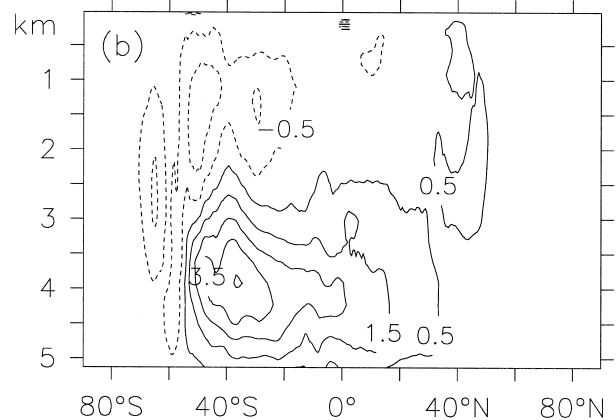
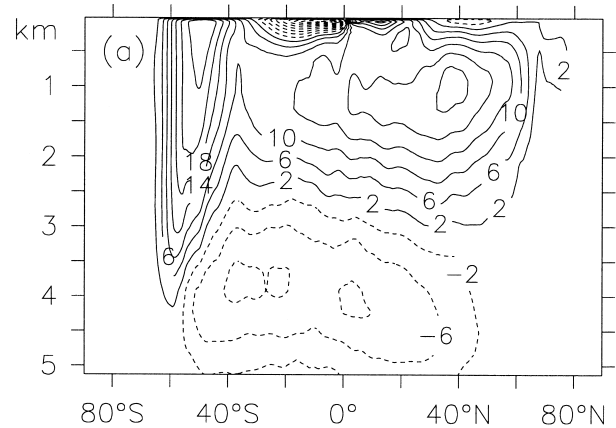


FIG. 6. Annual average meridional overturning streamfunction (in Sv) due to the mean flow at year 100; (a) case D, contour interval 4 Sv; and (b) case D - case C, contour interval 1 Sv.

changes. The primary region is that of the ACC, where the eddy-induced transport is a maximum because the largest gradients of temperature and salinity at 500 m in the world's oceans occur in this region. Another region is the far North Atlantic, which is affected by changes in the thermohaline circulation caused by the different eddy parameterizations.

In summary, the ocean-alone experiments with the new physics parameterizations have a much smaller drift in their area-averaged temperature profiles away from the observations used as initial conditions. This improvement is largest in the upper ocean between the depths of 200 m and 1 km. Does this improvement also occur in the ocean component simulations using a fully coupled climate model?

#### 4. Coupled model setup and results

The atmosphere component of the coupled model is the updated version of the Community Climate Model, version 3 (CCM3), which was used in the CSM-1.3 (see Boville et al. 2001). It includes a prognostic cloud water formulation and several additional greenhouse gases compared to the version used in CSM-1.0 and PCM-1,

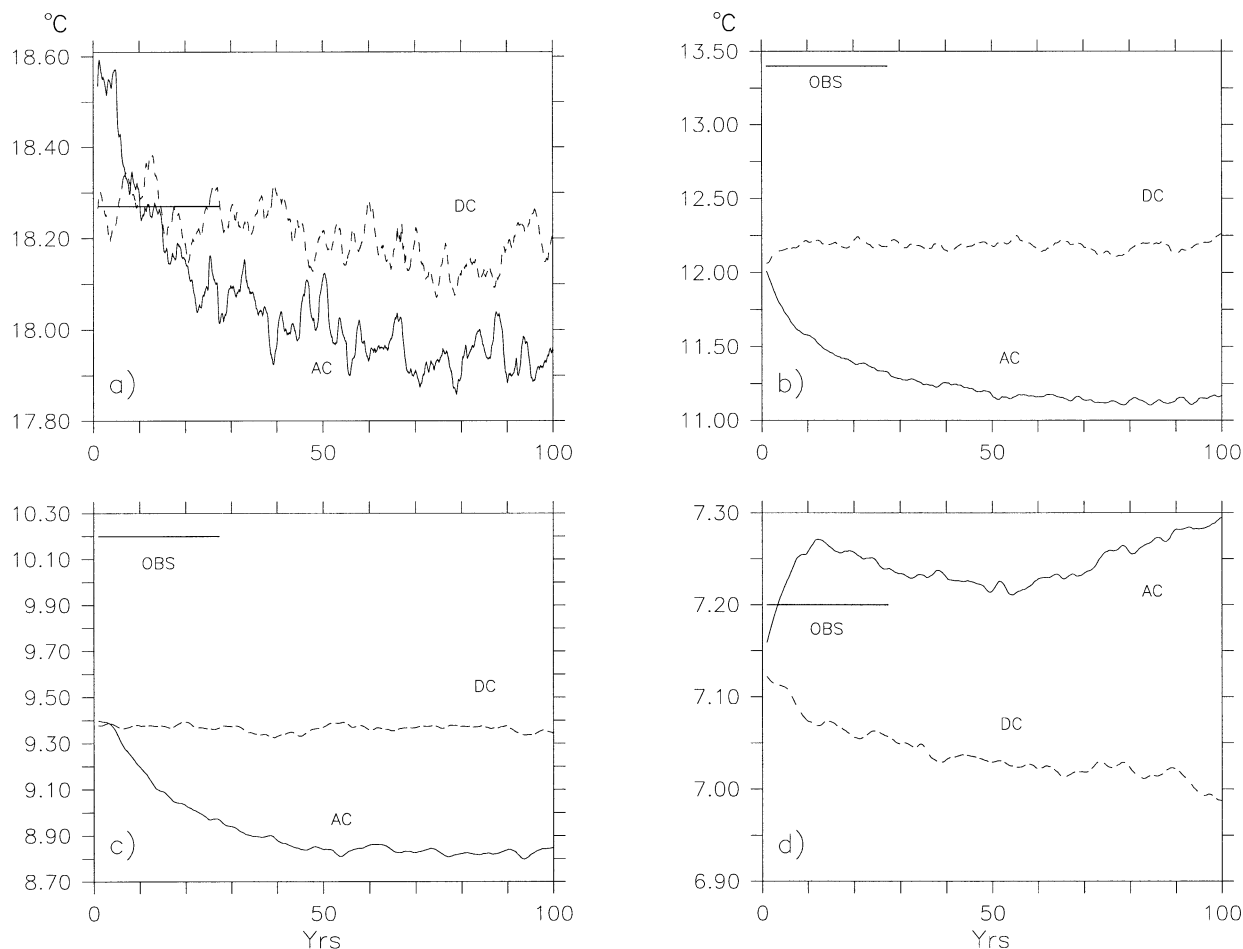


FIG. 7. The area-averaged potential temperature ( $^{\circ}\text{C}$ ) at depths of (a) 0, (b) 147, (c) 289, and (d) 520 m from cases AC (solid) and DC (dashed) plotted against time (yr). The Levitus et al. value is also shown.

which is described in Kiehl et al. (1998). The horizontal resolution is about  $2.8^{\circ}$  because T42 truncation is used, and there are 18 vertical layers. One change has been made to this component; the cloud liquid water path over the ocean is decreased by 60% where the atmospheric surface temperature is colder than 272 K. It increases linearly back to its full value as the surface temperature increases to 277 K. This significantly increases the amount of solar radiation reaching the surface ocean and sea ice in the polar regions, correcting a known deficiency of the CCM3. This has a considerable effect on the distribution of sea ice. The land component is the land surface model used in both the CSM-1.0 and PCM-1 (see Bonan 1998), and it uses the same T42 grid as the atmosphere. The ocean component has slightly enhanced resolution compared to the ocean-alone integrations. The upper-ocean resolution has been improved because there are now eight equal levels in the upper 100 m, and 40 levels in total. The horizontal grid now has  $384 \times 320$  grid points, and the zonal resolution is uniform. The sea-ice model is new and will be fully documented elsewhere as it is an early version

of the sea-ice component for the Community Climate System Model. It consists of the elastic–viscous–plastic ice rheology of Hunke and Dukowicz (1997), an ice thickness distribution model described in Bitz et al. (2001), and a thermodynamic model with an explicit brine-pocket parameterization based on the work of Bitz and Lipscomb (1999). The sea-ice model uses the same displaced North Pole grid as the ocean component.

The river runoff scheme in these coupled integrations was used in the PCM-1 and is described in Branstetter (2001). It resolves the river basins at the same T42 grid used in the land component. Surface fluxes are exchanged between the atmosphere, land, and sea ice every hour, but only daily averaged fluxes are exchanged between the ocean and the other model components. As in the PCM-1 integrations, precipitation plus runoff minus evaporation over the ocean and sea ice is balanced every day by multiplying the precipitation by a spatially constant factor. The time average of this factor over the coupled integrations is very close to one, the value it should take if freshwater is conserved within the fully coupled system. However, there is not exact conser-

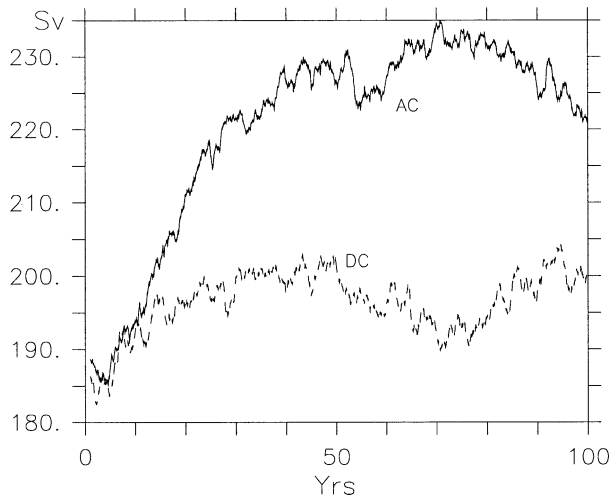


FIG. 8. The mass transport (Sv) through Drake Passage from cases AC (solid) and DC (dashed) plotted against time (yr).

vation of freshwater; the land component has sources or sinks over lakes, and the older free surface formulation used in this POP ocean component is very weakly nonconservative of freshwater. However, the drifts in the globally averaged ocean salinity are very small and do not affect any of the conclusions made in section 5.

Two 100-yr integrations were performed with ocean parameterizations corresponding to cases A and D in section 3, which will be labeled cases AC and DC to denote coupled integrations. This tests the original PCM-1 and the new ocean physics in fully coupled mode. The initial conditions for these integrations are taken from the end of an earlier 80-yr fully coupled integration using the new ocean physics, during which some ocean and sea-ice parameter values were optimized. In particular, the coefficient  $\alpha$  in Eq. (1) was changed to 0.02, and this value is retained in case DC. The drifts in the ocean component away from the initial conditions will be much smaller in case DC than case AC, because the 80-yr run used the new ocean physics. However, the Levitus values will also be shown on time series figures from the coupled integrations, so that drifts away from the observational values can be easily seen.

The globally averaged potential temperature in case DC reduces by  $0.12^{\circ}\text{C}$  over the 100 yr from the initial condition of  $3.48^{\circ}\text{C}$ . This continues the reduction in the previous 80-yr coupled run from the Levitus value of  $3.81^{\circ}\text{C}$ . The reduction in case AC is considerably smaller, being  $0.03^{\circ}\text{C}$  over 100 yr. The rate at which the ocean gains or loses heat is determined by how well the heat flux at the ocean surface is balanced in the coupled model, and this depends upon all the components, especially the atmosphere. However, the ocean-alone and fully coupled runs are consistent in that the net heat flux into the ocean is larger with the old physics than with the new physics.

Figure 7 is a plot of the area-averaged temperature

at the surface and depths of 147, 289, and 520 m against time from the two coupled integrations. Figure 7a shows that, after 100 yr the SST in case AC is about  $18.0^{\circ}\text{C}$ , whereas in case DC it is  $18.2^{\circ}\text{C}$ ; the Levitus value is  $18.27^{\circ}\text{C}$ . Figures 7b,c show large differences in the trends at 147- and 289-m depth. At 147 m, the temperature in case AC has cooled by  $2.2^{\circ}\text{C}$  from the Levitus value to  $11.2^{\circ}\text{C}$ , but in case DC it has cooled by  $1.2^{\circ}\text{C}$  to  $12.2^{\circ}\text{C}$ . At 289 m, the temperature in case AC has cooled by  $1.35^{\circ}\text{C}$  from the Levitus value to  $8.85^{\circ}\text{C}$ , but in case DC it has cooled by  $0.85^{\circ}\text{C}$  to  $9.35^{\circ}\text{C}$ . Figure 7d shows that at 520-m depth, both cases have a very small trend away from the Levitus value of  $7.2^{\circ}\text{C}$ , although it is larger in case DC. Thus, the strong cooling trend in the upper 400 m that occurred in the original version of the PCM-1 (see Fig. 3 of Meehl et al. 2001) is very significantly reduced with the new ocean physics.

A consequence of the better upper-ocean temperature profile in case DC is that the amplitude of interannual SST variability in the tropical Pacific is reduced a little compared to case AC. The reason is that warmer water is upwelled from shallow depths in case DC, which reduces the SST variability. The amplitude of this tropical Pacific SST variability in case DC is somewhat lower than the observed estimate, even though the background vertical diffusivity is realistically small [see section 2a, and Meehl et al. (2001)].

Another ocean quantity that is known to be rather sensitive to the effect of unresolved eddies is the strength of the ACC (see Gent et al. 2001). One reason is that the ACC is the only ocean current that circumnavigates the globe, and it is known that considerable heat and freshwater transports across it are accomplished by ocean eddies. The advection due to the eddies in the GM90 parameterization tends to oppose mean flow advection in the ACC, and the flattening of the isopycnals with the GM90 scheme leads to a lower mass transport by the ACC. Despite including the GM90 scheme, the Drake Passage transport in the CSM-1.0 300-yr coupled integration increased to 240 Sv (see Fig. 4 of Danabasoglu 1998). However, this coupled run used a much too large roughness length between the atmosphere and sea ice. When this was corrected, the Drake Passage transport reduced to 180 Sv in the control run of the CSM-1.3 version (see Boville et al. 2001). This value is still considerably larger than the best observational estimates, which are  $130 \pm 13$  Sv (see Whitworth et al. 1982; Whitworth 1983). The PCM-1 coupled run used the correct atmosphere to sea-ice roughness length, but the Drake Passage transport increased to 270 Sv at the end of the 300-yr run when using the case AC ocean physics (see Washington et al. 2000). It is expected that the Drake Passage transport will be smaller with the new physics that includes the GM90 parameterization. Figure 8 shows the mass transport through Drake Passage against time from the two coupled integrations and confirms this expectation. The case

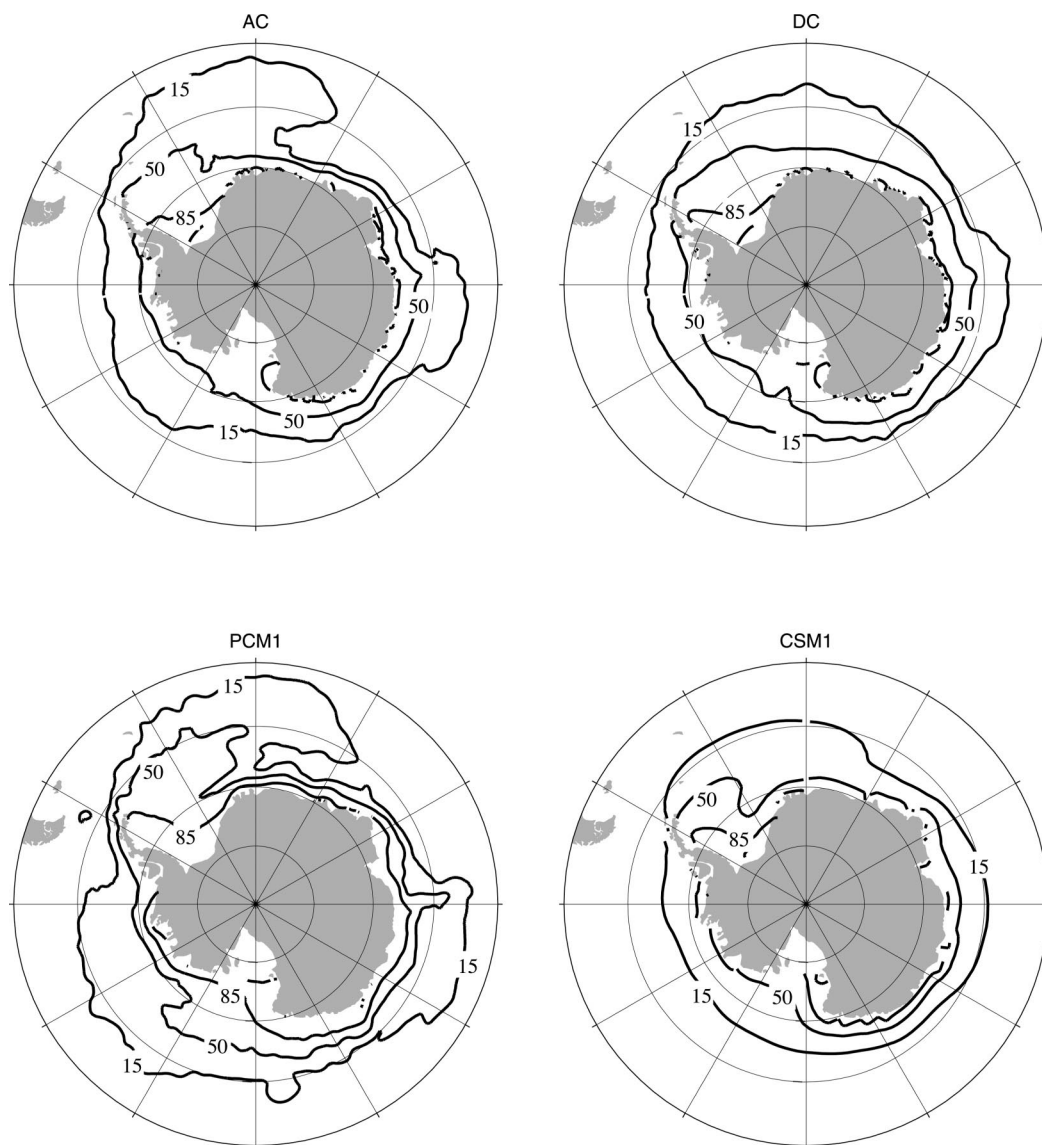


FIG. 9. Annual average Antarctic percentage sea-ice concentrations: (a) case AC, (b) case DC, (c) PCM-1 control, and (d) CSM-1.0 control.

AC transport increases during the first 75 yr to greater than 230 Sv, but reduces thereafter, and is about 220 Sv after 100 yr. In contrast, after a small initial increase the case DC transport is relatively steady with an average value of 197 Sv over the last 50 yr of the integration.

Ocean mixing parameterizations also influence the sea-ice simulation in coupled climate integrations. Vertical mixing in the upper ocean and poleward heat transport in the ocean affect the amount of heat available to melt ice and hence influence the thickness and horizontal extent of the sea ice. However, the area covered by sea ice in the two coupled simulations shows very little sensitivity to the ocean model parameterizations compared here. At about  $13 \times 10^{12} \text{ m}^2$  in the Northern

Hemisphere and  $9.3 \times 10^{12} \text{ m}^2$  in the Southern Hemisphere, the mean area is within 15% of that estimated from microwave data by Cavalieri et al. (1997). However, the ice is considerably more extensive, usually defined as the ocean area with 15% or more sea-ice coverage, in case AC than case DC in the Southern Hemisphere. Figure 9 shows the annual mean Antarctic sea-ice concentrations from cases AC, DC, PCM-1, and CSM-1.0. The sea-ice cover in case DC is closest to satellite observations of this quantity. The Antarctic sea-ice distribution in case DC is an improvement over the CSM-1.0 simulation, which has too little ice, and the PCM-1 and case AC simulations, which have too extensive an Antarctic sea-ice distribution.

Figure 10 shows the time evolution of the annual

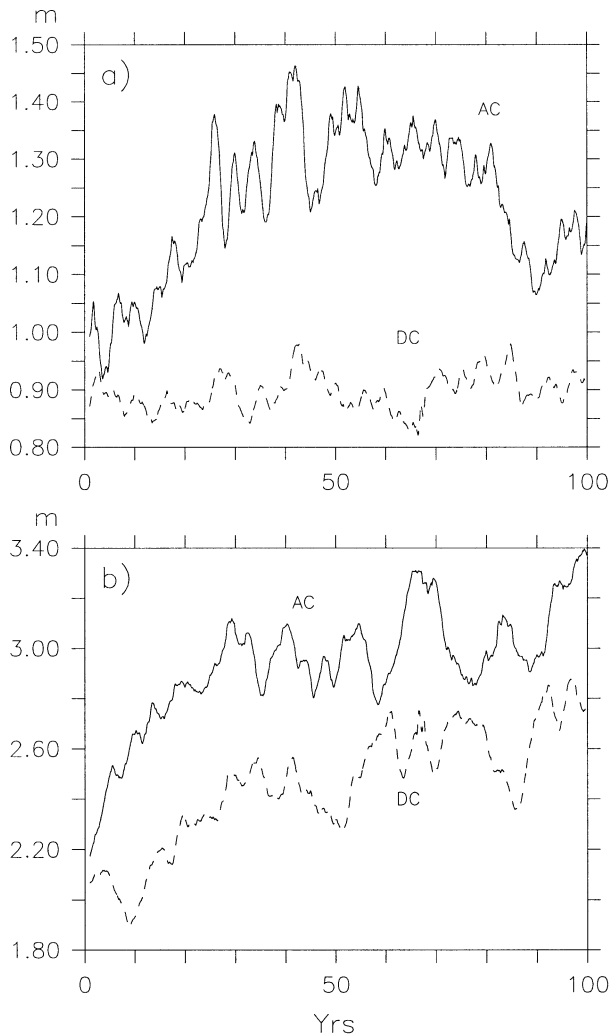


FIG. 10. Sea-ice thicknesses (m) for (a) the Antarctic and (b) the Arctic from cases AC (solid) and DC (dashed) plotted against time (yr).

mean sea-ice thickness for the ice-covered portions of each hemisphere in the two coupled integrations. There is considerable interannual and decadal variability in the ice thickness, but quite small trends over the last 50 yr of the integrations. In the Antarctic, the average sea-ice thickness is about 0.9 m in case DC, but 1.2 m in case AC over the last 25 yr. The sea-ice thickness in the Southern Hemisphere is not well measured, but the thinner ice in case DC is probably more realistic. The average ice thickness in the Arctic is about 2.6 m in case DC, and 3.0 m in case AC over the last 25 yr. Both values are within the range of measured sea-ice drafts of 1.8–3.1 m, depending on the decade, reported in Rothrock et al. (1999).

The sea-ice distribution is influenced by the new ice formed over open water, which is referred to as frazil ice growth. The frazil ice growth rates are quite different in cases AC and DC, and their seasonal march in both

hemispheres is shown in Fig. 11. In the Antarctic, the larger frazil ice production in case AC accounts for the more extensive thin ice shown in Fig. 9. In the Arctic, the frazil ice growth in case AC is about 25% greater than in case DC, but this represents only 4 or 5 cm of ice growth over a year. In the Arctic, the bottom ablation and accretion rates are much larger than the frazil ice growth rate, but they are almost exactly the same in the two coupled runs. Both runs have about 0.5 m of bottom ablation over a year, which is consistent with observations during the Surface Heat Budget of the Arctic (SHEBA) experiment in the western Arctic from October 1997 through September 1998 (see Perovich et al. 1999). Both coupled runs have 1.2 m of accretion over a year, which is considerably higher than recent measurements, which range from 0.45 to 0.75 m (see Lindsay 1998; Perovich et al. 1999). However, the model net freezing rate, which is the top and bottom ablation plus accretion, is similar to those summarized in Steele and Flato (1999).

The difference in Arctic frazil ice production in cases AC and DC can probably be attributed to different upper-ocean temperatures profiles. The sea ice is primarily insulated from the warmer subsurface temperatures by the stable stratification caused by the low-salinity surface layer. However, vertical mixing does provide a small upward heat transfer that affects the rate of ice formation. Figure 12 shows the case AC and DC temperature profiles averaged over the GIN Sea and the Arctic basin. Temperatures in the GIN Sea are 1°–1.5°C warmer in case DC than case AC between 100 and 700 m. The warmer temperatures in case DC will increase the upward heat transfer and reduce the frazil ice growth compared to case AC (see Fig. 11). In both cases, the temperatures in the GIN Sea over the upper 1 km are 2°–3°C warmer than the improved observational climatology of Steele et al. (2001). In the Arctic basin, the temperatures in case DC are 0.2°–0.5°C warmer than case AC from 100- to 700-m depth (see Fig. 12b). The temperatures in both cases are similar to the climatology from the surface to 300 m, but 1°–2°C warmer than the climatology below 500 m.

In summary, the Antarctic sea-ice concentration in case DC is somewhat less extensive and has an average thickness of 0.9 m, both of which are improvements over the case AC simulation. The Arctic sea-ice concentration is very similar in cases AC and DC, and the average thicknesses of 3 and 2.6 m are both within the observational range. Sea-ice extent in coupled models depends on the poleward heat transport by the ocean component. The Northern Hemisphere poleward heat transports are very close in cases AC and DC, which is consistent with the Arctic sea-ice concentrations being very similar. Thus, in these two coupled integrations the sea ice is improved, especially in the Antarctic, using the newer ocean component parameterizations.

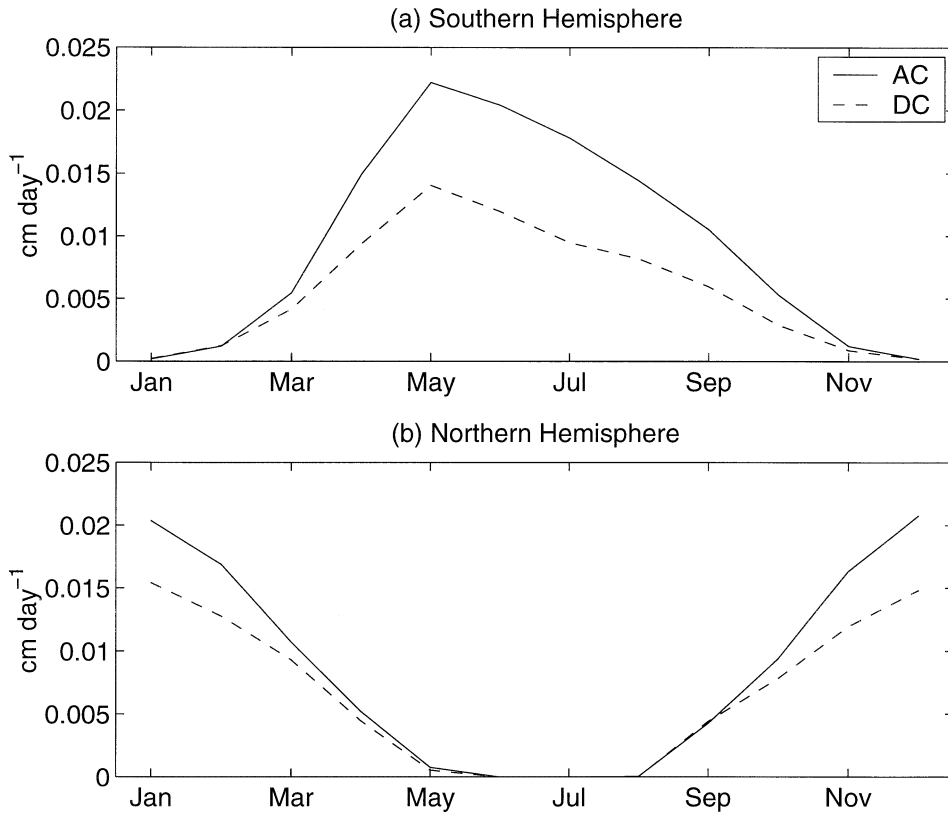


FIG. 11. Frazil ice production rate (in  $\text{cm day}^{-1}$ ) plotted against month for (a) the Antarctic and (b) the Arctic for case AC (solid) and case DC (dashed).

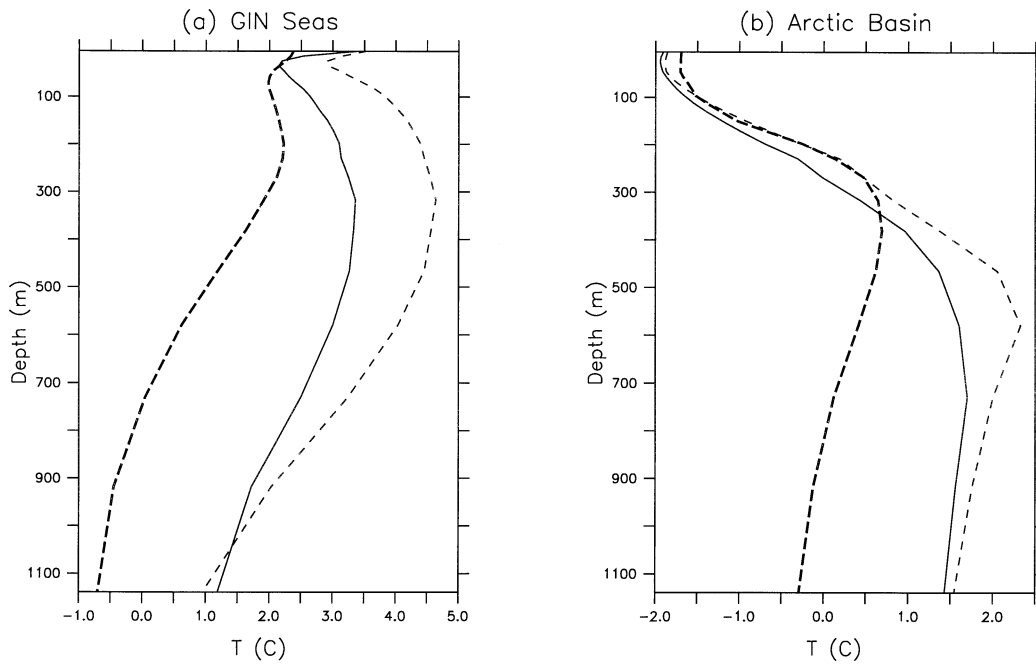


FIG. 12. Annual average temperatures ( $^{\circ}\text{C}$ ) over the upper 1.1 km: (a) GIN Sea and (b) Arctic basin for case AC (solid), case DC (dashed), and the Steele et al. observations (thick dashed).

## 5. Discussion and conclusions

The vertical temperature profile in the ocean component of the parallel climate model (PCM) has a strong cold bias of greater than 2°C over the upper 400 m in its control run (see Meehl et al. 2001). Section 3 shows the results of changing the ocean vertical mixing and eddy parameterization schemes in this ocean component to the KPP and GM90 schemes used in the climate system model (CSM). These are ocean-alone integrations forced by observations, in which the area averaged SST is strongly constrained by the forcing. The first conclusion of this work is that biases in the upper-ocean temperature profile down to 500 m are much smaller with the KPP and GM90 schemes than with the older physics used in the PCM. Some of this improvement comes from using the KPP vertical mixing scheme, rather than the PP scheme, but most of the improvement comes from using the GM90 scheme, rather than horizontal mixing of tracers. It is well known that the GM90 scheme improves results from coarse-resolution, non-eddy-resolving ocean models used for climate work, but this is a clear demonstration of the improvement well into the eddy-permitting regime, with an average horizontal resolution of about 0.7°.

Section 3 also contains results of using the VMHS modification of the GM90 scheme. This allows the GM90 coefficient to vary in time and space depending on the local baroclinicity of the flow. The second conclusion is that the VMHS scheme makes only small changes to the global solution properties compared to the GM90 scheme, which uses a constant coefficient. However, the scheme can result in much larger local changes in the regions of the ACC and far North Atlantic, where the isopycnal diffusivity takes large values. These are the same regions that show the largest changes when using the GM90 scheme instead of horizontal tracer mixing. The isopycnal diffusivity using the VMHS scheme, shown in Fig. 4, has a quite realistic spatial pattern when compared to eddy kinetic energy distributions from very high-resolution ocean simulations. Given that the scheme is almost no increase in computational cost over the GM90 scheme, it should be used in eddy-permitting ocean models for climate.

Section 4 contains results from two fully coupled integrations; the first using the original PCM ocean physics and the second using the KPP and VMHS schemes. The third conclusion is that the improvements in the upper-ocean temperature profile seen in the ocean-alone integrations carry over to the fully coupled integrations. The drift in the temperature profile down to 400 m is substantially reduced in the integration with the KPP and VMHS schemes.

The sea-ice distributions in the two fully coupled integrations are also analyzed in section 4. The integration using the KPP and VMHS schemes shows an improved ice extent around Antarctica and thinner sea ice in both hemispheres. These changes are due, in part, to the dif-

ferent rates of frazil ice production in both hemispheres. The rate of Arctic frazil ice production is influenced by the warmer upper-ocean temperatures in the GIN Sea and Arctic basin in the integration using the KPP and VMHS schemes. However, the sea-ice distribution in coupled climate integrations is sensitive to both sea-ice parameterizations and the atmospheric forcing, in addition to being dependent on the ocean simulation. Thus, obtaining a good sea-ice distribution in coupled models depends on having good atmosphere, ocean, and sea-ice components.

*Acknowledgments.* The National Center for Atmospheric Research is sponsored by the National Science Foundation. Anthony Craig was funded by a cooperative agreement between NCAR and the Climate Change Prediction Program of the U.S. Department of Energy, which also provided much of the computer time used. Thanks also to Thomas Bettge, Brian Kauffman, and Gary Strand who oversaw the coupled integrations and produced several figures.

## REFERENCES

- Bitz, C. M., and W. H. Lipscomb, 1999: An energy-conserving thermodynamic model of sea ice. *J. Geophys. Res.*, **104**, 15 669–15 677.
- , M. M. Holland, M. Eby, and A. J. Weaver, 2001: Simulating the ice-thickness distribution in a coupled climate model. *J. Geophys. Res.*, **106**, 2441–2463.
- Bonan, G. B., 1998: The land surface climatology of the NCAR land surface model coupled to the NCAR Community Climate Model. *J. Climate*, **11**, 1307–1326.
- Boville, B. A., and P. R. Gent, 1998: The NCAR Climate System Model, version one. *J. Climate*, **11**, 1115–1130.
- , J. T. Kiehl, P. J. Rasch, and F. O. Bryan, 2001: Improvements to the NCAR CSM-1 for transient climate simulations. *J. Climate*, **14**, 164–179.
- Branstetter, M. L., 2001: Development of a parallel river transport algorithm and applications to climate studies. Ph.D. thesis, University of Texas at Austin, 102 pp.
- Bryden, H. L., D. H. Roemmich, and J. A. Church, 1991: Ocean heat transport across 24° in the Pacific. *Deep-Sea Res.*, **38**, 297–324.
- Cavaleri, D. J., P. Gloersen, C. L. Parkinson, J. C. Comiso, and H. J. Zwally, 1997: Observed hemispheric asymmetry in global sea ice changes. *Science*, **278**, 1104–1106.
- Danabasoglu, G., 1998: On the wind driven circulation of the uncoupled and coupled NCAR Climate System Ocean Model. *J. Climate*, **11**, 1442–1454.
- Gent, P. R., and J. C. McWilliams, 1990: Isopycnal mixing in ocean circulation models. *J. Phys. Oceanogr.*, **20**, 150–155.
- , F. O. Bryan, G. Danabasoglu, S. C. Doney, W. R. Holland, W. G. Large, and J. C. McWilliams, 1998: The NCAR Climate System Model global ocean component. *J. Climate*, **11**, 1287–1306.
- , W. G. Large, and F. O. Bryan, 2001: What sets the mean transport through Drake Passage? *J. Geophys. Res.*, **106**, 2693–2712.
- Gordon, C., C. Cooper, C. A. Senior, H. Banks, J. M. Gregory, T. C. Johns, J. F. B. Mitchell, and R. A. Wood, 2000: The simulation of SST, sea ice extents and ocean heat transports in a version of the Hadley Centre coupled model without flux adjustments. *Climate Dyn.*, **16**, 147–168.
- Hall, M. M., and H. L. Bryden, 1982: Direct estimates and mechanisms of ocean heat transport. *Deep-Sea Res.*, **29**, 339–359.

- Hunke, E. C., and J. K. Dukowicz, 1997: An elastic–viscous–plastic model for sea ice dynamics. *J. Phys. Oceanogr.*, **27**, 1849–1867.
- Kiehl, J. T., J. J. Hack, G. B. Bonan, B. A. Boville, D. L. Williamson, and P. J. Rasch, 1998: The National Center for Atmospheric Research Community Climate Model: CCM3. *J. Climate*, **11**, 1131–1149.
- Large, W. G., J. C. McWilliams, and S. C. Doney, 1994: Oceanic vertical mixing: A review and a model with a nonlocal boundary layer parameterization. *Rev. Geophys.*, **32**, 363–403.
- , G. Danabasoglu, S. C. Doney, and J. C. McWilliams, 1997: Sensitivity to surface forcing and boundary layer mixing in the NCAR CSM ocean model: Annual-mean climatology. *J. Phys. Oceanogr.*, **27**, 2418–2447.
- Levitus, S., R. Burgett, and T. P. Boyer, 1994: *Salinity*. Vol. 3, *World Ocean Atlas 1994*, NOAA Atlas NESDIS 3, 99 pp.
- Lindsay, R. W., 1998: Temporal variability of the energy balance of thick Arctic pack ice. *J. Climate*, **11**, 313–333.
- Macdonald, A., and C. Wunsch, 1996: An estimate of global ocean circulation and heat fluxes. *Nature*, **382**, 436–439.
- McCartney, M. S., and R. A. Curry, 1993: Transequatorial flow of Antarctic bottom water in the western Atlantic Ocean: Abyssal geostrophy at the equator. *J. Phys. Oceanogr.*, **23**, 1264–1276.
- Meehl, G. A., P. R. Gent, J. M. Arblaster, B. Otto-Bliesner, E. Brady, and A. P. Craig, 2001: Factors that affect the amplitude of El Niño in global coupled climate models. *Climate Dyn.*, **17**, 515–526.
- Pacanowski, R. C., and S. G. H. Philander, 1981: Parameterization of vertical mixing in numerical models of the tropical oceans. *J. Phys. Oceanogr.*, **11**, 1443–1451.
- Perovich, D. K., and Coauthors, 1999: *SHEBA: Snow and Ice Studies*. CD-ROM, version 1.0.
- Roberts, M. J., and D. Marshall, 1998: Do we require adiabatic dissipation schemes in eddy-resolving ocean models? *J. Phys. Oceanogr.*, **28**, 2050–2063.
- Rothrock, D. A., Y. Yu, and G. A. Maykut, 1999: Thinning of the Arctic sea-ice cover. *Geophys. Res. Lett.*, **26**, 3469–3472.
- Smith, R. D., J. K. Dukowicz, and R. C. Malone, 1992: Parallel ocean circulation modeling. *Physica D*, **60**, 38–61.
- , M. E. Maltrud, F. O. Bryan, and M. W. Hecht, 2000: Numerical simulation of the North Atlantic Ocean at 1/10°. *J. Phys. Oceanogr.*, **30**, 1532–1561.
- Steele, M., and G. M. Flato, 1999: Sea ice growth, melt, and modeling: A survey. *The Arctic Ocean Freshwater Budget*, E. L. Lewis, Ed., NATO Science Series, Vol. 2, Kluwer Academic, 623 pp.
- , R. Morley, and W. Ermold, 2001: PHC: A global ocean hydrography with a high quality Arctic Ocean. *J. Climate*, **14**, 2079–2087.
- Trenberth, K. E., and J. M. Caron, 2001: Estimates of meridional atmosphere and ocean heat transports. *J. Climate*, **14**, 3433–3443.
- Visbeck, M., J. Marshall, T. Haine, and M. Spall, 1997: Specification of eddy transfer coefficients in coarse-resolution ocean circulation models. *J. Phys. Oceanogr.*, **27**, 381–402.
- Washington, W. M., and Coauthors, 2000: Parallel Climate Model (PCM) control and transient simulations. *Climate Dyn.*, **16**, 755–774.
- Whitworth, T., 1983: Monitoring the transport of the Antarctic Circumpolar Current in Drake Passage. *J. Phys. Oceanogr.*, **13**, 2045–2057.
- , W. D. Nowlin, and S. J. Worley, 1982: The net transport of the Antarctic Circumpolar Current through Drake Passage. *J. Phys. Oceanogr.*, **12**, 960–971.